Electron Microscopy Investigations of Nanostructured Ce/Mn Oxides for Catalytic Wet Oxidation

8 AUTHORS, INCLUDING:

Ana B Hungria
Universidad de Cádiz
90 PUBLICATIONS   2,549 CITATIONS

SEE PROFILE

M. A. Cauqui
Universidad de Cádiz
54 PUBLICATIONS   1,190 CITATIONS

SEE PROFILE

José M. Rodríguez-Izquierdo
Universidad de Cádiz
86 PUBLICATIONS   1,546 CITATIONS

SEE PROFILE

Jose J Calvino
Universidad de Cádiz
173 PUBLICATIONS   3,418 CITATIONS

SEE PROFILE

Electron Microscopy Investigations of Nanostructured Ce/Mn Oxides for Catalytic Wet Oxidation

José A. Pérez-Omil,*,† Juan J. Delgado,† Widad Ouahbi,† Ana B. Hungría,† Nigel Browning,‡ Miguel A. Cauqui,† José M. Rodríguez-Izquierdo,† and José J. Calvino†

Departamento de Ciencia de los Materiales e Ingeniería Metalúrgica y Química Inorgánica, Facultad de Ciencias, Universidad de Cádiz, Campus Río San Pedro, Puerto Real, 11510-Cádiz, Spain, and Department of Chemical Engineering and Materials Science, University of California—Davis, One Shields Avenue, Davis, California 95616

A series of Ce/Mn oxides has been characterized using a variety of complementary transmission electron microscopy techniques to obtain nanometer scale information on the structure, chemical composition, and oxidation states of the different phases present in this extremely complex system. The phases have been identified to be α-Mn_2O_3, β-MnO_2, mixed-valence manganese oxides (Mn_3O_4 and Mn_5O_8), and Ce—Mn mixed oxides in different proportions depending on the Ce/Mn atomic ratio. A correlation between the nanostructure of this composite system and its catalytic activity for the wet oxidation of phenol, as a model contaminant, is proposed.

1. Introduction

Ce/Mn oxides have been extensively investigated in recent years due to their excellent chemical properties as environmental catalysts. Studies devoted to the removal of pollutants from water by catalytic wet oxidation (CWO),[1–10] oxidation of CO or small hydrocarbon molecules,[11–14] low temperature oxidation of diesel soot,[15] elimination of nitrogen oxides,[14,16–19] catalytic oxidation of ammonia in supercritical water (SCW)[20] and, more recently, the production of hydrogen by splitting of the water molecule using concentrated solar thermal energy have been reported.[21] Different methods have been used for the preparation of Ce/Mn mixed oxides, such as impregnation,[16,22] different variants of coprecipitation,[1–5,8,9,11–19,23] sol—gel,[12] and combustion.[21,22] In all cases a Ce/Mn composite oxide is finally obtained. Only when the combustion method is used for molar manganese contents [Mn/(Ce + Mn)] lower than 20% does a solid solution, $Ce_{1-x}Mn_xO_{2-\delta}$, seem to be synthesized as the main product.[21,22] The rest of the preparation methods cited above give rise to complex mixtures of phases with different structures and oxidation states; including several manganese oxides and fluorite related cerium oxides. The final phase distribution and therefore the resulting properties of the material are a function of the Ce/Mn molar composition, preparation method, and temperature used for the calcination of the precursors.[2,8,9,11,12,16,17,22]

A synergetic effect between manganese oxides and cerium oxides phases has been reported in all the studied cases, regardless of the specific application, with the chemical activity of the Ce/Mn oxides being higher than that corresponding to the pure manganese or cerium oxides. Maximum activity is usually achieved for manganese molar compositions ranging between 30% and 50%. Macroscopic techniques have been intensively used for the characterization of Ce/Mn oxides, such as X-ray diffraction, Fourier transform infrared spectroscopy (FTIR), electron paramagnetic resonance (EPR), X-ray photo-

electron spectroscopy (XPS), and thermogravimetrical and adsorption/desorption techniques. Very few electron diffraction or transmission electron microscopy (TEM) studies have been reported.[3,5,8] Therefore, there is a lack of information in the literature about the structure, chemical composition, and oxidation states of the Ce/Mn oxides on the nanometer scale, which is key to understanding the details of the spatial distribution of the different phases as well as their mutual interactions. Only with this information can a proper understanding of the origin of the synergetic effect in this family of materials be obtained.

Taking these ideas into consideration, the main goal of this work has been to perform a complete characterization of a series of Ce/Mn oxides, using a variety of complementary TEM techniques, to establish a correlation between the nanostructure and the catalytic activity of this system. High resolution electron microscopy (HREM) and selected area electron diffraction (SAED) have allowed us to explore the crystal structure and morphology of the different oxides as well as the structural relationships between them. X-ray energy dispersive spectroscopy (X-EDS) has been used to obtain information about the chemical composition of the materials with nanometer spatial resolution. This has allowed us to distinguish the manganese phases from the cerium ones, and to estimate Ce/Mn molar ratios in cases where a solid solution of the oxides is formed. The newest generation of microscopes can also work in scanning transmission electron microscopy (STEM) mode. The possibility of scanning an electron probe (with a diameter of the order of 0.2 nm) across the sample allows *Z* (atomic number) contrast images to be recorded using a high angle annular dark field (HAADF) detector. Likewise, when the electron beam is positioned at one specific point on the sample, it is possible to obtain information (with subnanometer resolution) of the chemical composition and oxidation states of the existing elements using electron energy loss spectroscopy (EELS). With this set of TEM/STEM techniques, we have explored the details of the structure of a series of Ce/Mn oxides, covering the whole range of Ce/Mn compositions, which were prepared by a

---

* Corresponding author. E-mail: jose.perez-omil@uca.es.
† University of Cádiz.
‡ University of California—Davis.

TABLE 1: Crystallographic Data for Manganese Oxides Phases

phase	mineral	comments	space group	ref
MnO		manganosite	NaCl-like	$Fm3\bar{m}$	30
Mn_3O_4	tetragonal	hausmanite	distorted spinel	$I4_1/amd$	29
	cubic		high temp (spinel)	$Fd3\bar{m}$	71
	orthorrombic	marokite	high pressure	$Pbcm$	72
Mn_2O_3	α-Mn_2O_3		distorted C-type Ln_2O_3	$Pbca$	28
	β-Mn_2O_3	bixbyite	nondistorted C-type Ln_2O_3. (1% Fe)	$Ia3$	28
	γ-Mn_2O_3		cation defect spinel	$Fd3\bar{m}$ related	32
Mn_5O_8			$Cd_2Mn_3O_8$-like	$C2/m$	36
MnO_2	β-MnO_2	pirolusite	rutile-like structure	$P4_2/mnm$	27
	γ-MnO_2		with 2×1 channels	Pbnm (ramsdellite)	73, 74
	α-MnO_2		with 2×2 channels	$I4/m$	75
Mn_2O_7			volatile	$P2_1/c$	76
$Mn(OH)_2$			$Mg(OH)_2$, brucite-like	$P3\bar{m}1$	77
MnOOH	α-MnOOH	groutite	α-AlOOH-like	$Pnma$	78
	γ-MnOOH	manganite		$P2_1/c$	38

standard coprecipitation method. The characterization data reported in this work allows us to achieve solid conclusions.

On the other hand, standard catalytic activity tests have been performed on this family of oxides for the total oxidation of organic carbon from model phenol solutions.[1,24] As mentioned above, special attention has been paid to understanding the origin of the synergetic effect observed in the catalytic activity for the CWO process.

A proper understanding of the whole set of data reported in this paper requires a consideration of all the crystallographic phases that could be potentially involved in the complex characterization problem we have dealt with. Thus, before going into the experimental details, we will conclude this introduction with a brief description of some structural questions specific to the materials we have studied. The large number of structures, oxidation states and polymorphs of manganese oxides make precise phase identification in this kind of system a difficult task; see Table 1. As an additional complication, we should recall that they can transform into each other depending on the redox nature, reducing or oxidizing, of the pretreatments to which they could be submitted during their synthesis, activation, or catalytic function.[25,26] For instance, β-MnO_2 (pyrolusite), with the rutile structure, is the most stable of the dioxides.[27] This phase can transform into α-Mn_2O_3 when heated in air at 680 °C. It later crystallizes in an orthorhombic unit cell that can be considered a distorted version of the C-type lanthanide oxide structure.[28] α-Mn_2O_3 decomposes in air at 830 °C into the tetragonal Mn_3O_4, known as hausmannite.[29] This is a spinel-like structure, distorted by the Jan−Teller effect, where manganese ions in oxidation states +2 and +3 coexist. Manganese monoxide, mangnosite, with a NaCl-like structure is obtained by heating this latter phase in air above 1700 °C.[30–32]

Noteworthy, the sequence of phases obtained by oxidation of the lower manganese oxides is more complex. MnO is easily oxidized in air to Mn_3O_4 at low temperature.[26] However, the transition from Mn_3O_4 to α-Mn_2O_3 is kinetically controlled.[33–35] This reaction may proceed through two metastable phases: γ-Mn_2O_3 as a first oxidation product and Mn_5O_8 in a second step. γ-Mn_2O_3 may be considered as a cation-defective spinel-like structure,[32] very closely related to the Mn_3O_4 structure. On the other hand, Mn_5O_8 is a mixed-valence oxide (manganese cations in oxidation states +2 and +4) isostructural to $Cd_2Mn_3O_8$ phase.[36] There are no data in the literature reporting the formation of β-MnO_2 from the oxidation in air of a lower manganese oxide; however, it can be easily obtained by oxidation of γ-MnOOH, manganite, at temperatures between 250 and 310 °C.[37,38]

The redox behavior of cerium oxides is quite different.[39,40] Cerium dioxide crystallizes into a cubic, fluorite-like, structure. The reduction of this oxide is accomplished by the formation of oxygen vacancies. At high temperature these vacancies become randomly distributed or aggregated in the form of microdomains. At low temperature, the oxygen vacancies get ordered, giving rise to intermediate phases that are superstructures of the original fluorite. All these phases have the same fcc-like sublattice of cations as in the initial fluorite structure of the dioxide.[40] In the last steps of reduction, a cubic C-type $Ce_2O_{3+\delta}$ is observed.[41] However, when the complete reduction of Ce^{4+} is achieved ($\delta = 0$), the trigonal A-Ce_2O_3, with hcp-like cations sublattice, is formed.[42]

Finally, concerning the system Ce/Mn, we need to recall that cerium oxide is known to form solid solutions with other metallic oxides such as PrO_2, TbO_2, ZrO_2, or La_2O_3, over a large range of compositions.[43] However, when a precipitate is obtained from a solution containing manganese and cerium ions, as we have mentioned, the result is different. In general, a Ce/Mn composite oxide is obtained. In this composite we should expect the presence of a fluorite-like oxide coexisting with several manganese oxides.

Having in mind this very complex map of crystallographic phases and structural relationships existing for cerium and manganese oxides, the major goal of this paper is to elucidate the structure and composition of a series of Ce/Mn composite oxides by using information provided by techniques with subnanometer scale spatial resolution, to understand the behavior of this system for the catalytic oxidation of model phenol solutions.

2. Experimental Section

The cerium−manganese composite oxides investigated were prepared by coprecipitation, using ammonia, from aqueous solutions containing manganese(II) and cerium(III) nitrates (Merck). The precipitates were filtered, washed using deionized water, and dried in an oven overnight at 100 °C. Once dried, the samples were calcined in air at 500 °C for 1 h. The Mn molar compositions of the resulting materials were, as confirmed by the inductively coupled plasma (ICP) technique,[24] approximately 5%, 15%, 50%, 85%, and 100% (pure manganese oxide). In the following we will refer to these samples as CM5, CM15, CM50, CM85, and CM100, respectively.

X-ray diffraction (XRD) analyses were performed on a Philips PW1820 diffractometer (Cu Kα radiation) operating at 40 kV and 40 mA and processed using Powder Cell software.[44]

Nanostructured Ce/Mn Oxides

J. Phys. Chem. C, Vol. 114, No. 19, 2010 **8983**
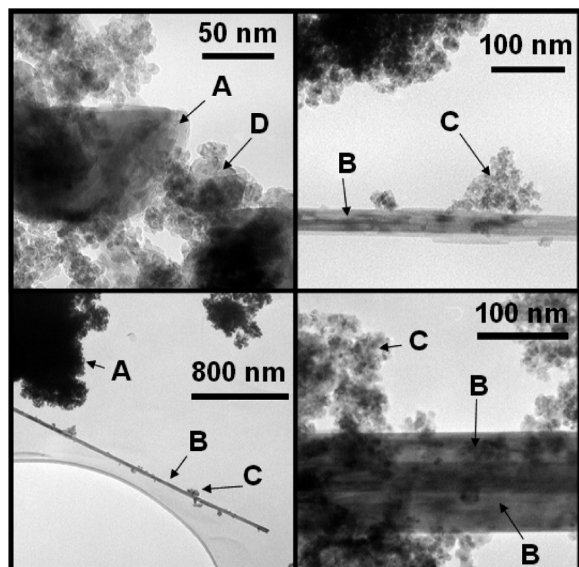
Figure 1. Typical TEM images from sample CM50 where the different cerium/manganese oxide nanostructures are labeled with the letters A, B, C, and D.

Figure 2. Experimental X-ray powder diffraction data from the cerium/manganese oxide samples. The diffraction peaks corresponding to α-Mn_2O_3 and the fluorite-like structure are marked with (O) and ($\square$), respectively.
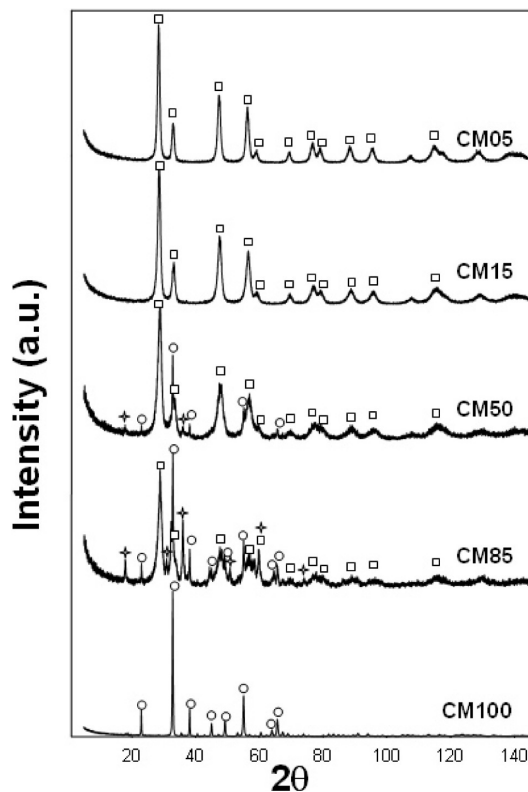
Temperature programmed reduction (TPR) experiments were performed in a flux of He using a mass spectrometer (MS) from VG (Sensorlab 200D) controlled by the software Quasar 6.1. The amount of sample used in these experiments was 200 mg, the He flow rate was 60 $cm^3 \cdot min^{-1}$ and the heating ramp was 10 $K \cdot min^{-1}$.

High resolution electron microscopy images were recorded in a JEOL 2000-EX, working at 200 kV with a structural resolution of 0.21 nm. X-EDS analysis was performed in a CM200-FEG microscope using an EDAX system. A TECNAI F20 microscope, equipped with a field emission gun (FEG), was used to record HAADF images and EELS data (energy resolution of 0.5 eV). Electron microscopy data were processed using Semper 6+ software and Digital Micrograph. HREM image simulations were performed using EMS software. Eje-Z and Rhodius software, developed at the University of Cádiz, were used for the interpretation of HREM images and modeling of the complex superstructures needed for image simulations.[45,46]

The catalytic reactions were carried out in a 500 mL autoclave originally charged with 250 mL of distilled water and 0.5−2.0 g of Ce/Mn oxide as catalyst. A concentrated solution of phenol was injected at the reaction temperature (80, 90, or 110 °C) and at a fixed pressure of oxygen (0.5 MPa). Total organic carbon (TOC) was measured after 15 min of reaction by using a Shimadzu TOC analyzer. The phenol conversion was determined at the same time by a gas chromatograph (GC 8000 Top Series from CE Instruments) equipped with a flame ionization detector (FID), very sensitive for analyzing organic compounds.

3. Results and Discussion

3.1. General Characterization and Catalytic Activity Measurements. Figure 1 depicts representative low magnification TEM images recorded on the studied samples. To a first approximation, the aggregates found in the different samples can be classified, according to their size and morphology, into four types of oxide particles, which we will name in the following as A, B, C, and D types. Type A particles correspond to large and rounded, nonfaceted, crystals, with sizes on the order of 100 nm. Type B crystals are those exhibiting a rodlike shape. The length of these rods ranges from several nanometers to several micrometers. A huge number of pretty small, well faceted, crystallites decorating the larger crystals' surfaces are observed all over the samples (type C). A minor fraction of crystals is also found whose size and morphology do not fit with any of the categories mentioned before (type D). As will be shown in section 3.5, these crystals correspond to mixed-valence manganese oxides. These four types of oxide particle crystals were observed for any Ce/Mn molar ratio, except for the sample CM100, pure manganese oxide, where only the first type (A), the large and rounded crystals, could be detected.

Figure 2 shows the powder X-ray diffraction data for all the studied samples. In the case of CM100 the diffraction pattern can be assigned to α-Mn_2O_3. No other phases could be observed. However, a fluorite-like structure, with diffraction peaks very close to the pure CeO_2 structure, is the only phase detected for samples CM05 and CM15. For the intermediate composition, sample CM50, in addition to the main peaks of α-Mn_2O_3 (20% weight) and fluorite-like phases (60% weight), other peaks can be observed that fit the *d* spacings of some manganese mixed-valence oxide structures, like Mn_5O_8 or tetragonal Mn_3O_4. Due to the low intensities of these weak peaks, precise phase identification could not be carried out. The presence of the Mn_3O_4 phase is more evident in the X-ray diffraction diagram of the CM85 sample, in which the contribution of the mixed-valence oxides is about 30% in weight.

Figure 3 shows temperature programmed reduction (TPR-MS) profiles ($m/q = 32$, O_2 signal) of the studied samples. Pure manganese oxide shows one reduction peak,[25] which is associated with the reduction of α-Mn_2O_3 to Mn_3O_4. For the Ce/Mn composite oxides, three new peaks at lower temperatures can
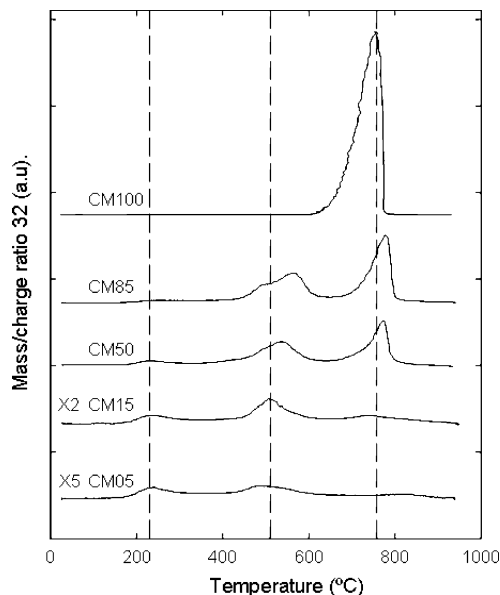
Figure 3. Temperature programmed reduction data ($m/q = 32$, O_2 signal, flux of He) from the investigated cerium/manganese oxide samples.

Figure 4. Effect of Ce/(Ce + Mn) ratio on phenol (A) and TOC (B) removal at different temperatures: 110 (●), 90 (▲), and 80 (◆) °C. Reaction time: 15 min. Initial phenol concentration: 500 ppm. Partial oxygen pressure: 0.5 MPa.

Figure 5. HREM image (a) and SAED pattern (b) corresponding to different crystals of CM100 sample. The HREM image is interpreted as α-Mn_2O_3 along the [111] zone axis. The SAED pattern corresponds to α-Mn_2O_3 along the [001] zone axis.
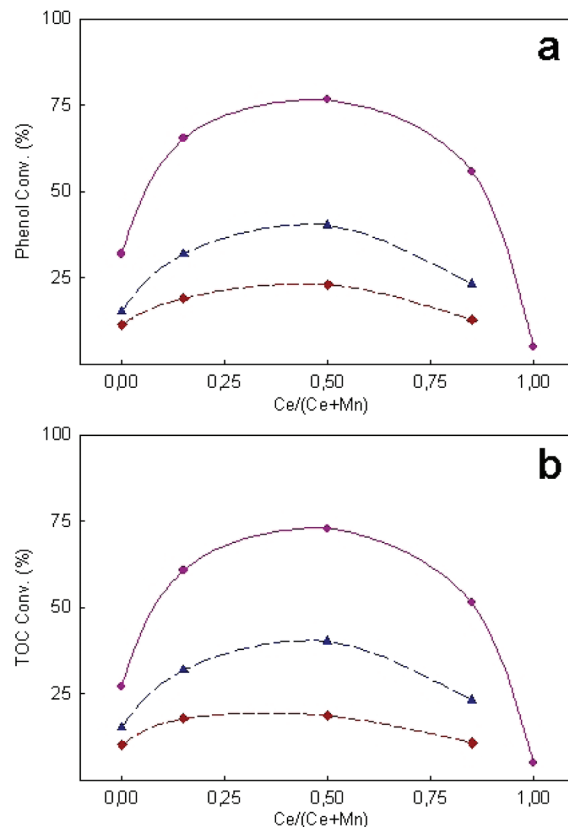
be distinguished, which may be attributed to the presence of other manganese oxides and fluorite-like phases.

On the other hand, catalytic activity tests have been performed for the oxidation of phenol in water (CWO) as a function of Mn content. Figure 4 shows the phenol conversion and the total oxidation of carbon (TOC) after 15 min of reaction at 0.5 MPa (PO_2) and different temperatures. In all the cases the maximum is achieved for sample CM50, which contains equimolar amounts of cerium and manganese. This clear synergetic effect found for the Ce/Mn composite oxides is in good agreement with those reported elsewhere.[1]

3.2. Characterization of the Rounded-Large Oxide Particles (Type A). This type of crystal is the only one we have observed by TEM in the pure manganese oxide sample, CM100. Their size ranges from 50 to 100 nm, and all of them look rounded. As already described in section 3.1, the X-ray diffraction diagram of this sample can be assigned to α-Mn_2O_3. Selected area electron diffraction (SAED) patterns and high resolution electron microscopy (HREM) images, recorded for a large number of oxide crystals in CM100 sample, confirm this result. Figure 5a shows a representative HREM image of this sample that can be unambiguously interpreted as α-Mn_2O_3 along the [111] zone axis. The experimental SAED pattern shown in Figure 5b, also from CM100, corresponds to α-Mn_2O_3 structure along the [001] zone axis.

TEM images also show the presence of this kind of oxide particles, large and rounded crystals, in samples CM15, CM50, and CM85, where both cerium and manganese ions are present. They should be responsible for the α-Mn_2O_3 diffraction peaks identified in the powder X-ray diffraction patterns, as shown in section 3.1. To confirm this structural analysis on the nanometer scale, we have performed some further TEM experiments. The interpretation of several SAED patterns and HREM images recorded from large-rounded crystals in these samples points again to a α-Mn_2O_3 structure. XEDS analysis indicates that the chemical composition of these crystals corresponds to a pure manganese oxide.

Figure 6 shows a representative HREM image of one of these crystals in sample CM15. The digital diffraction pattern (DDP),
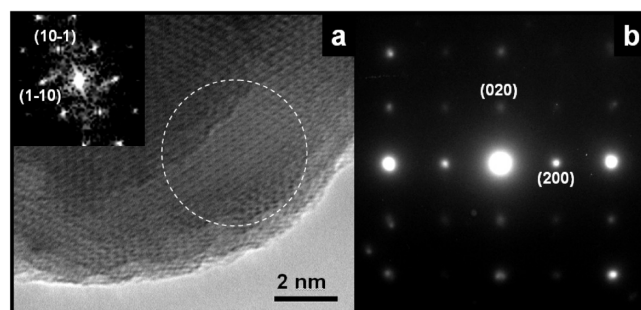
inset in Figure 6c, can be interpreted as due either to α-Mn_2O_3 structure along the [132] direction or to β-Mn_2O_3 along [132] (Figure 6a,b, respectively). The simulated dynamical electron diffraction patterns for these two cases look very similar, but they can be distinguished by the presence of a small intermediate spot (0.54 nm) in the direction of the reflection ($2\bar{2}2$) for the α-Mn_2O_3 structure. This intermediate spot is easily observed in the experimental image, so we can finally reject β-Mn_2O_3 and assign the experimental image to a α-Mn_2O_3 structure along the [132] direction.

This interpretation provides valuable information about the nature of this manganese oxide phase. While α-Mn_2O_3 corresponds to an orthorhombic (distorted cubic) structure, β-Mn_2O_3 corresponds to a perfect cubic oxide. This cubic structure is

Nanostructured Ce/Mn Oxides

J. Phys. Chem. C, Vol. 114, No. 19, 2010 **8985**
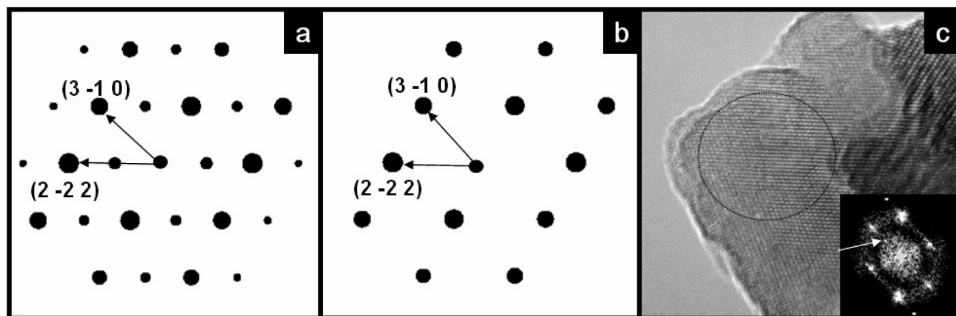
Figure 6. Simulated dynamical electron diffraction patterns of α-Mn_2O_3 (a) and β-Mn_2O_3 (b) along the [132] zone axis. Experimental HREM image (c) of the CM15 sample that can be interpreted as α-Mn_2O_3 in the [132] zone axis orientation.
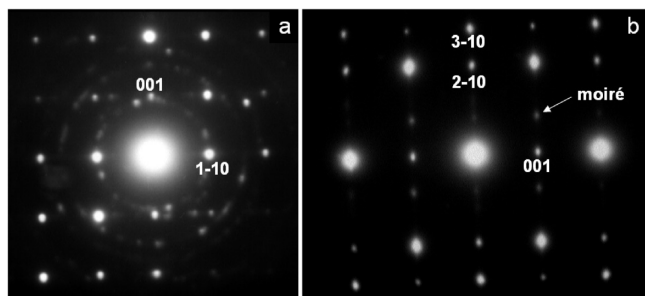

Figure 7. Experimental SAED patterns corresponding to different nanorods in sample CM50, indexed using the β-MnO_2 structure. The rings observed in (a) are due to the presence of fluorite-like nanocrystals (type C oxide particles). In (b) the diffraction spots corresponding to the double diffraction process (moiré) between two adjacent β-MnO_2 nanorods are identified.

usually stabilized with dopants, usually iron, as happens in the mineral bixbyite.[28] The presence of this intermediate spot in our experimental images points, therefore, to a pure, undoped oxide and allows us to rule out, as a first approximation, the presence of a small amount of cerium ions inside type A crystallites. This result is also in good agreement with the analysis of the powder X-ray diffraction data, which show no shift of the peaks attributable to the α-Mn_2O_3 phase for samples with different Ce/Mn molar ratios.

3.3. Characterization of the Rodlike Oxide Particles (Type B). We can observe oxide particles with rodlike shape in the whole range of Ce/Mn compositions, with the exception of sample CM100, which only contains α-Mn_2O_3 manganese oxide. The length of these rods ranges from several nanometres to several micrometers. XEDS analysis reveals that these rods do not contain cerium, therefore corresponding to a pure manganese oxide.

Figure 7a shows a SAED of one of these nanorods in sample CM50, which can be assigned to β-MnO_2 along the [110] direction, Mn_5O_8 along [$\bar{1}$02], or tetragonal Mn_3O_4 along [031]. The dynamical electron diffraction simulations corresponding to these three zone axis are quite similar, as depicted in Figure 8. This clearly indicates that a reliable assignment to a particular manganese oxide phase cannot be done in this orientation by a simple inspection[5] of the experimental diffraction pattern.

Figure 7b shows a more complex SAED pattern recorded on two stacked nanorods. The diffraction spots corresponding to each individual crystal as well as spots due to double diffraction effects (moiré spots) are observed. As illustrated in Figure 8, this complex SAED pattern can be initially interpreted as the overlap of two crystals of (1) β-MnO_2 along the [120] and [130] zone axes, (2) Mn_5O_8 along [10$\bar{4}$] and [10$\bar{6}$] zone axes, or (3) Mn_3O_4 along the [013] and [375] zone axes. Once more, reliable assignment to a particular phase cannot be made.
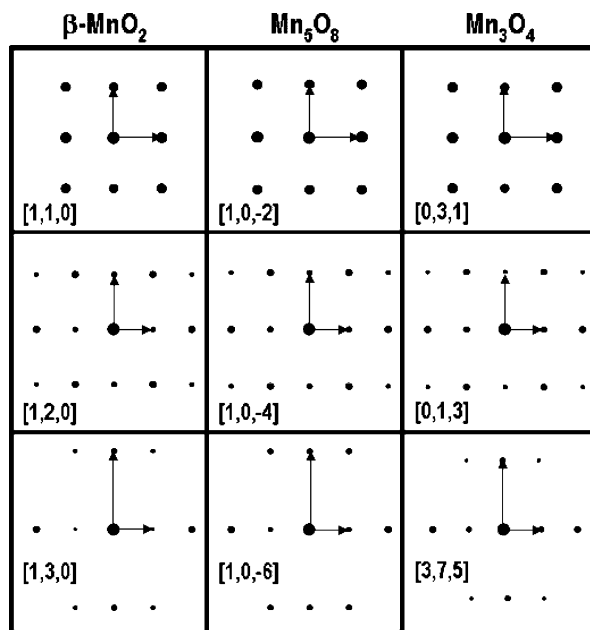
Figure 8. Simulated dynamical electron diffraction patterns of β-MnO_2, Mn_5O_8, and Mn_3O_4 along several orientations.
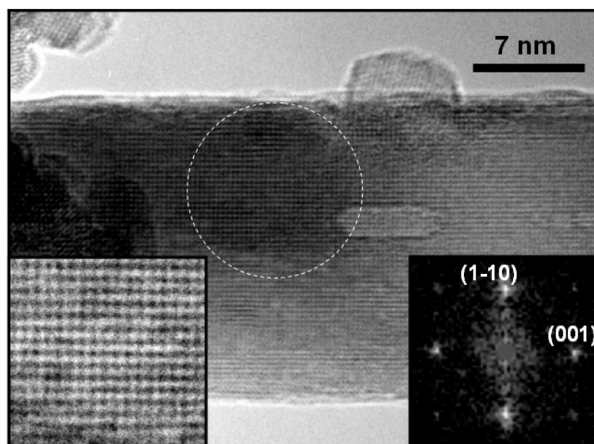
Figure 9. HREM image, selected area of interest, and the corresponding digital diffraction pattern (DDP) of a nanorod taken from the CM85 sample. The indexes correspond to β-MnO_2 along the [110] zone axis.

To get further insight into the chemical and crystallographic nature of these type B phase nanocrystals, HREM analysis was performed. Figure 9 shows a HREM image with atomic resolution of one of the nanorods recorded from sample CM85. This image can be interpreted as due to β-MnO_2 along the [110]
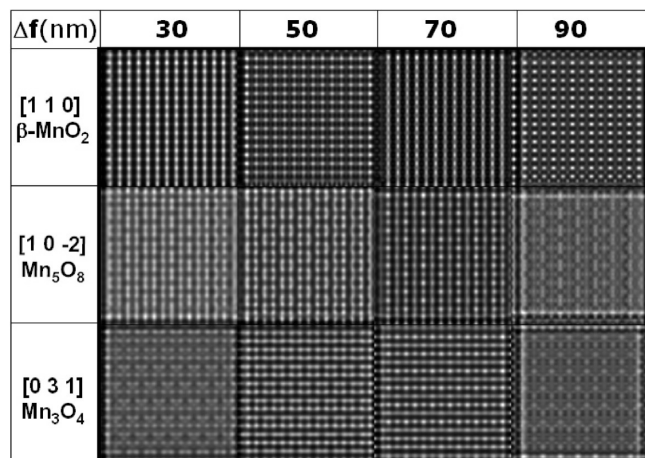
Figure 10. Simulated HREM images calculated at different defocuses for a 5 nm thickness using the characteristics of the JEOL 2000-EX microscope. High tension: 200 kV. Spherical aberration: 0.7 mm. Objective aperture: 12 nm^{-1}. Spread of focus: 10 nm. Semiconvergence angle: 1.2 mrad.
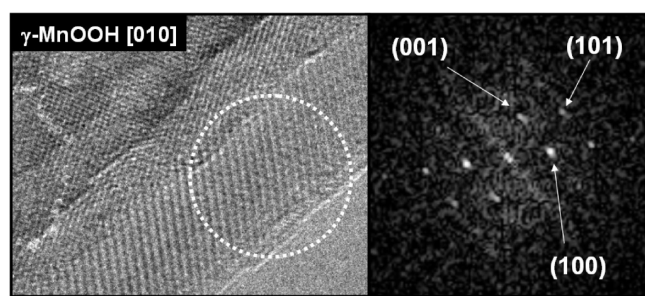
Figure 11. Experimental HREM image of a nanorod recorded from the sample CM50 precursor. The DDP obtained from the selected area can be interpreted as γ-MnOOH along the [010] zone axis. The nanorod growths are along the (101) reciprocal direction.

direction, Mn$_5$O$_8$ along [$\bar{1}$02], or Mn$_3$O$_4$ along [031], in good agreement with electron diffraction data in Figure 7a. Thickness-defocus maps of simulated HREM images were calculated for these three possibilities. Figure 10 shows a selection of the most significant images obtained in this image simulation study. Note that, although apparently very similar, differences can be detected in their fine contrast features. From the whole set of calculations, the images corresponding to the β-MnO$_2$ structure along [110] are those exhibiting the closest match with the experimental ones. According to this interpretation, the axis of the nanorod corresponds to the c axis of the tetragonal, rutile-type, unit cell of this structure.

A characterization of the samples before the thermal treatment in air at 500 °C has been performed to determine more precisely at which step in the Ce/Mn composite oxide synthesis the formation of the nanorods takes place. HREM images recorded from these samples show nanorods very similar in dimensions and morphology to the ones found in the final samples, i.e., after calcination. However, in contrast to that observed in the calcined samples, these nanorods are surrounded by amorphous material and oxide nanoparticles.

Figure 11 shows a HREM image close to the surface of a nanorod observed in sample CM50 before calcination. The digital diffraction pattern shows two 0.5 nm spots at an angle of 65.0°. These features do not match those of a β-MnO$_2$ phase but, instead, those of γ-MnOOH along [010]. In this case the axis of the nanorod is aligned with the (101) direction. This
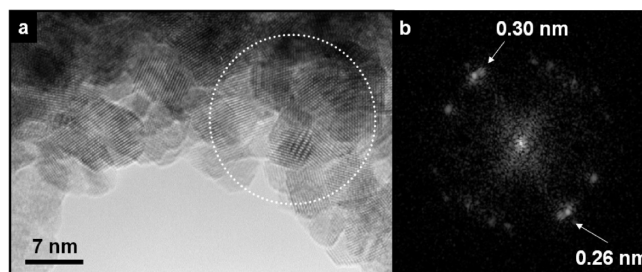
Figure 12. Typical HREM image (a) and the DDP corresponding to a selected area (b) of a CM15 sample showing nanocrystals of phase C.

direction, indexed according to the standard space group $P2_1/c$, is equivalent by a change of basis to the (001) direction of the B-centered setting space group named B2$_1$/d, which is that routinely used to describe the γ-MnOOH structure.[38,47] Recall that the B-centered unit cell can be transformed to the primitive-standard one using the following relationship $\langle e| = \langle e_B| \cdot P$, where $\langle e|$ and $\langle e_B|$ correspond to the standard and B-centered basis sets, respectively, and P is the following transformation matrix (by rows): {1/2, 0, −1/2 // 0, 1, 0 // 1/2, 0, 1/2}.

Taking into account that the β-MnO$_2$ nanorods are aligned to the (001) reciprocal direction we can establish the following structural relationship between the phases appearing before and after calcination:

γ-MnOOH (101) (standard setting) //
    γ-MnOOH (001) (B-centered setting) // β-MnO$_2$ (001)

This relationship is in good agreement with that reported elsewhere[47] and denotes a topotaxial transformation of the γ-MnOOH nanorods to β-MnO$_2$ nanorods during the thermal treatment at 500 °C, along the [010] zone axis:[38,47−51]

γ-MnOOH [010] (standard setting) //
    γ-MnOOH [010] (B-centered setting) // β-MnO$_2$ [010]

Taking into account these results, the most reliable assignment of the SAED patterns in Figure 7b is that considering crystals of a β-MnO$_2$ phase. In fact, two β-MnO$_2$ stacked nanorods rotated 8.15° through the [001] axis can fully explain the overlap of the β-MnO$_2$ [120] and β-MnO$_2$ [130] zone axes, and the formation of the observed moiré spots. The conclusions obtained by the interpretation of the HREM images and SAED patterns of the nanorods will be supported by the EELS data presented in section 3.6.

3.4. Characterization of the Oxide Nanoparticles (Type C). In all the CeO$_x$/MnO$_x$ samples we have prepared, except in CM100, it is possible to observe a huge amount of nanocrystals ranging in size from 2 to 4 nm. The lattice spacing and angles measured in DDPs corresponding to these nanoparticles are in good agreement with a fluorite-like structure with lattice parameter of 0.52 nm, as shown in Figure 12. This value is slightly shorter than that of pure CeO$_2$, 0.54 nm, suggesting the incorporation of some manganese in the form of solid solution; i.e., these particles would correspond to a Ce/Mn mixed oxide.

To have more quantitative information about the chemical composition of these oxide nanoparticles, extensive XEDS data were acquired from areas 10−50 nm in size on regions of the samples where only this type of particle was observed. The

Nanostructured Ce/Mn Oxides

J. Phys. Chem. C, Vol. 114, No. 19, 2010 **8987**
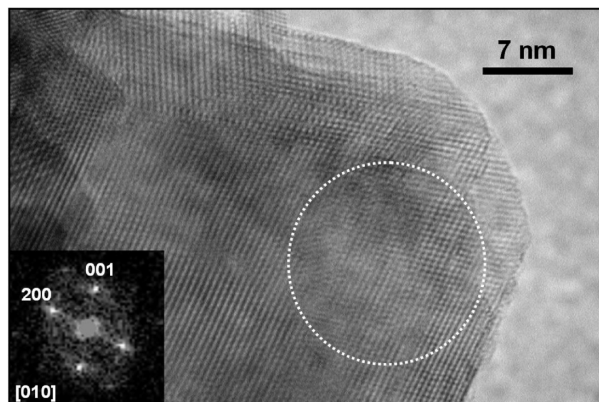
Figure 13. HREM image of a crystal registered in sample CM50. It can be interpreted as Mn_5O_8 along the [010] direction.

Figure 14. Experimental HAADF image taken from the CM50 sample. Some oxide nanorods can be observed among the rest of nanocrystals.

results show clearly the presence of both cations, Ce and Mn, in the oxide nanoparticles in a Ce/Mn molar ratio, which varies slightly from point to point. These data confirm the formation of a Ce/Mn mixed oxide solid solution with a nonhomogeneous composition.

The average value of Mn content in these mixed-oxide type phase for the different samples are approximately the following molar fractions: 10% in CM15, 15% in CM50, and 20% in CM85. These data denote a clear trend: the content of Mn in the mixed oxide nanocrystals increases as does the total content of Mn in the sample. This result is in good agreement with the analysis of the powder X-ray diffraction data, Figure 2, which shows a shift toward higher angle of the peaks attributable to the fluorite-like phase as the manganese content increases. On the other hand, there is a solubility limit of manganese into the fluorite matrix of cerium oxide. From the samples we have studied, it seems that the maximun Mn content that can incorporate into the oxide nanoparticles is around 20%.

3.5. Characterization of the Mixed-Valence Manganese Oxides (Type D). In all the samples we have studied, with the exception of sample CM100, there is always a fraction of crystals that cannot be assimilated, either by size or by morphology, to any of the phases described previously. HREM and SAED data recorded on these crystals can be interpreted as due to Mn_3O_4 or Mn_5O_8. These two phases are quite interesting because they contain manganese ions in two oxidation states: +2 and +3 or +2 and +4, respectively. Figure 13 shows a HREM image obtained from the CM50 sample. The digital diffraction pattern inset shows two diffraction spots (0.46 and 0.48 nm) at an angle of 72°, which can be unambiguously interpreted as the Mn_5O_8 structure along the [010] direction. The fraction of these mixed-valence manganese oxide crystals is significant in the CM85 sample, in good agreement with the X-ray diffraction data shown in section 3.1, but their contribution in CM50, the sample showing the highest catalytic activity, is very small.

3.6. Electron Energy Loss Spectroscopy (EELS) Data. We carried out a set of experiments using the transmission electron microscope in STEM-HAADF mode on the CM50 sample. Using this mode, we are able to acquire images, Figure 14, where the contrast is sensitive to chemical composition varia-tions (Z-contrast[52]). Additionally, the fine electron beam used in this mode (just a few angstroms in diameter) can be stopped on a spot to record an electron energy loss spectrum.[53] From the analysis of the fine structure (ELNES) of these spectra, it is possible to retrieve information about the chemical composition
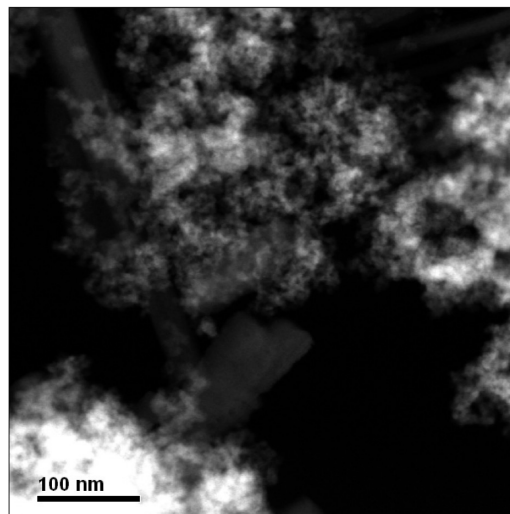
and the electronic structure of the material, more specifically the oxidation state of the elements in the analyzed area.

Figure 15 shows a series of EELS spectra recorded on crystallites corresponding to the different phases present in CM50. Thus, Figure 15a-A and Figure 15b-A depict the O−K and $Mn-L_{2,3}$ EELS signals from a large and rounded oxide particle (type A). The fine structure of this spectrum is quite similar to that reported for α-Mn_2O_3.[54,55] This is in good agreement with the structural analysis commented on above.

More interesting information may be inferred from the data shown in Figure 15a-B and Figure 15b-B. These show O−K and $Mn-L_{2,3}$ ELNES recorded from an oxide nanorod. The fine structure details of this spectrum fit with those reported for β-MnO_2.[54−56] It is clear from these nanoanalytical results that the previous assignment made on the basis of the detailed comparison of the structure of the rods before and after calcination is fully correct.

The spectra recorded from the nanorods have enough intensity and quality to be used as internal patterns of Mn in the oxidation state +4. In accordance with this, the position of the $Mn-L_3$ and $Mn-L_2$ white lines in these spectra can be fixed to 644.0 and 654.2 eV, respectively. From these values we can estimate the chemical shifts taking place in the white lines of manganese ions for other oxidation states; see Table 2. Thus, using this calibration criterion, the exact positions of the white lines in the ELNES of Figure 15b-A are 642.4 and 653.8 eV. Therefore there is a chemical shift of 1.6 eV, to lower energies, between the spectra recorded from a nanorod and the one recorded from a large rounded oxide particle, which is consistent with the change in the oxidation state of manganese from +4 to +3 reported elsewhere.[54,57,58]

Another interesting parameter that is sensitive to the oxidation state of manganese is the L_3/L_2 white line intensity ratio when the intensity is measured by integration over an energy window centered at the maximum of the white lines. These intensities are subtracted using a variation of the method proposed by Pearson.[59,60] From a set of EELS spectra taken from the nanorods, the value of this ratio averages to 1.9. We should expect changes in this value when the oxidation state of manganese deviates from +4. Thus, the L_3/L_2 intensity ratio measured from ELNES included in Figure 15b-A is 2.28. According to reported data,[54,61−64] this increment is consistent
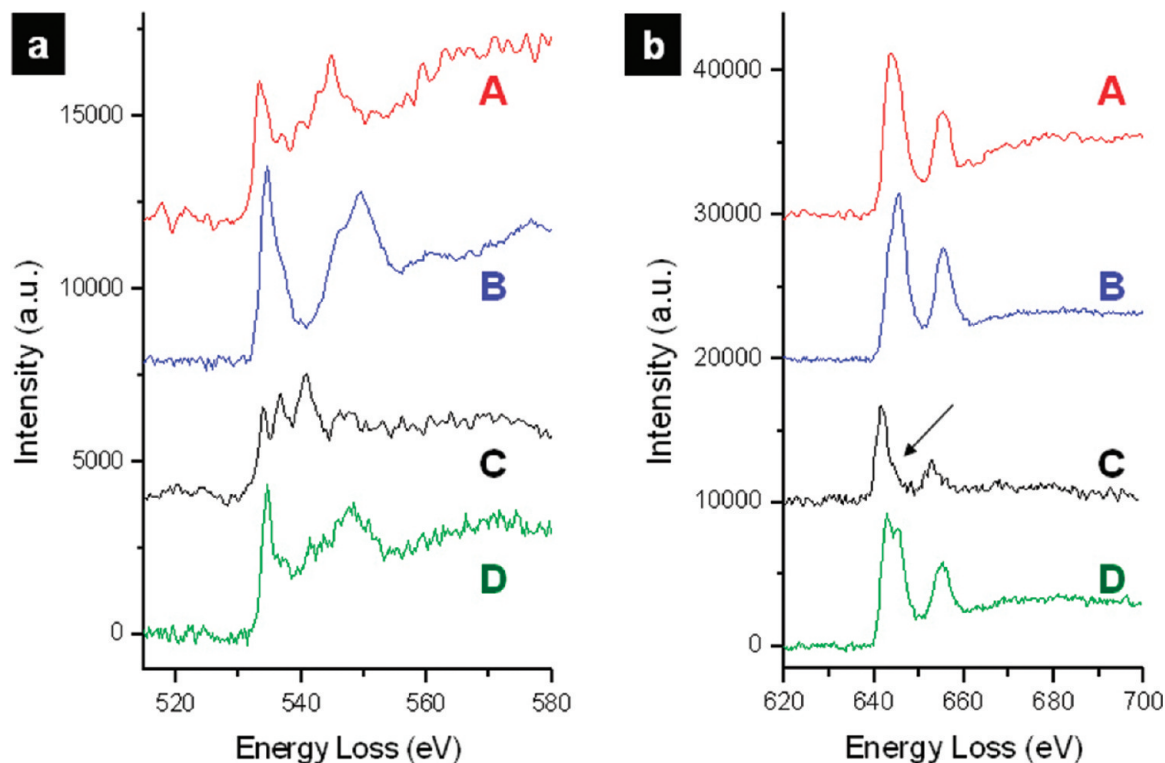
Figure 15. Experimental ELNES signals corresponding to O−K (a) and Mn-$L_{2,3}$ (b) edges from typical A-, B-, C-, and D-type manganese/oxide nanostructures.
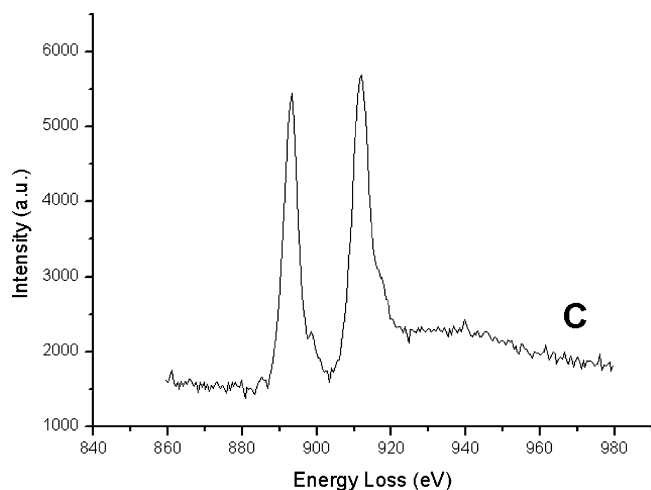
Figure 16. Experimental ELNES signal corresponding to the Ce-$M_{4,5}$ edge from typical C-type cerium/manganese nanoparticles. This ELNES has been extracted from the same electron energy loss spectrum as the one shown in Figure 15b-C.

TABLE 2: Mn-L_2 and Mn-L_3 Energy Loss Data from Sample CM50

type	oxid state	L_3 (eV)	L_2 (eV)	ΔL_3 (eV)	L_3/L_2	phase
B	+4	644.0	654.2	0.0	1.90	β-MnO$_2$
A	+3	642.4	653.8	1.6	2.28	α-Mn$_2$O$_3$
C	+2	641.0	652.3	3.0	3.60	Ce$_{1-x}$Mn$_x$O$_{2-x}$
D	+2	641.6	664.1	2.5	2.17	Mn$_5$O$_8$
	+4	644.1		0.1		

with the presence of manganese(III) in α-Mn$_2$O$_3$. The small difference between our L_3/L_2 ratios and other values, reported previously for the transition from the oxidation state +4 to +3,

is due to the details of the method used to extract the white line intensities.[59]

Applying quantitative analysis to the EELS spectra in which both O−K edge and Mn-$L_{2,3}$ edges are included, a Mn/O molar ratio may also be estimated. The average value of this ratio obtained from the spectra recorded from a number of nanorods is 0.52, which is very close to the nominal value of 0.50 for a MnO$_2$ stoichiometry. Considering once more these spectra as reference, an accurate width of the integration window to perform a reliable Mn/O ratio analysis could be fixed.

Spectra recorded from type C oxide nanoparticles contain three major signals: O−K, Mn-$L_{2,3}$ and Ce-$M_{4,5}$ edges, Figure 15a-C, Figure 15b-C, and Figure 16, respectively. These three signals exist in the EELS spectra even when a probe size of 0.2 nm is used. This fact clearly confirms that this phase is a real solid solution mixed oxide, involving a mixture of manganese and cerium ions at atomic scale in the nanocrystals, in good agreement with XEDS data presented above. The local variations of the intensity ratio between the Mn-$L_{2,3}$ and Ce-$M_{4,5}$ signals suggests that the composition of the solid solution changes from site to site, possibly due to some Mn clustering in the oxide nanocrystals.[65] The fine structure of the Ce-$M_{4,5}$ edge, Figure 16, corresponds to an oxidation state of +4.[66,67]

The comparison of a large number of pairs of EELS spectra, recorded consecutively from a nanorod and then from a region where only oxide nanoparticles were observed, indicates a chemical shift of 3.0 eV between the Mn-L_3 edges in both type of crystals; see Table 2. After fine calibration, using the position of the Mn-L_3 and Mn-L_2 white lines of β-MnO$_2$ as reference, the position of the peaks observed in Figure 15b-C are 641.0 and 652.3 eV, respectively. The large chemical shift found for the main white line (Mn-L_3) is very significant.[54,55,61,63,68] XAS experiments reported in the literature offer valuable information to be considered.[58] They describe an L_3 chemical shift of

1.0−2.0 eV for a change in the oxidation state of manganese from +4 to +3, and an additional chemical shift of 1.5−2.0 eV for a change from +3 to +2. In both cases the chemical shift is always lower than or equal to 2.0 eV for just one unit of change in the oxidation state. Taking into account this information and the oxidation state of manganese in the nanorods, which is +4, the chemical shift of 3.0 eV, observed when we go from the nanorods to the oxide nanoparticles, indicates that the oxide nanoparticles contains manganese in oxidation state +2. This is also in good agreement with the small shoulders appearing at the right side of the Mn-L_3 white lines in the ELNES of the oxide nanoparticles (marked with an arrow in Figure 15b-C), which is characteristic of manganese in oxidation state +2.

Also noteworthy, the value of the L_3/L_2 intensity ratio for the spectra taken from the oxide nanocrystals rises up to 3.60. Although, as already stated, the absolute values of these ratios are very sensitive to the method used to extract the white line intensities from the spectra,[59] 3.60 is a value very close to the one reported by other authors which have analyzed the fine structure of reference oxides for MnO.[54,55,61,63,64,68−70]

In spite of the inhomogeneous distribution of Mn in the oxide nanocrystals, we have performed a quantitative analysis from a set of EELS recorded on sample CM50. The average value of Mn molar content we have obtained is 0.11, which is consistent with the XEDS experiments performed with a larger electron probe (50 nm); see section 3.4. So, we can propose $Ce_{0.89}Mn_{0.11}O_{1.89}$ as an average chemical formula for the nanocrystals in sample CM50. To fix the oxygen content, we have considered that the oxidation states of Ce and Mn were +4 and +2, respectively.

Finally Figure 15a-D and Figure 15b-D show the ELNES recorded for a crystal that could not be identified as any of the other three (A, B, C) types of oxides. The white lines corresponding to the Mn-L_3 edge split into two peaks, indicating the presence of manganese in more than one oxidation state; see Table 2. However, the corresponding O−K edge does not match the one reported in the literature for the spinel-like Mn_3O_4 structure (manganese +2 and +3 mixed-valence oxide).[55,68] Taking into account the actual position of the two Mn-L_3 peaks (641.6 and 644.1 eV), we have tentatively assigned this spectrum to a Mn_5O_8 phase, where manganese ions are in the oxidation states +2 and +4, a guess that is in good agreement with our previous interpretation of HREM images, section 3.5.

4. Discussion

The whole set of data presented and analyzed in this work clearly evidence the great influence of the presence of Ce^{3+} ions when we are carrying out a precipitation of Mn^{2+} in a solution using ammonia. Thus, when pure $Mn(NO_3)_2$ is used during the synthesis, the final product obtained after calcination at 500 °C is α-Mn_2O_3, sample CM100. However, when the starting solution contains $Mn(NO_3)_2$ and $Ce_2(NO_3)_3$, the final material is a mixture of several phases that contains not only α-Mn_2O_3 crystals and a nanostructured Ce/Mn mixed oxide but also the β-MnO_2 phase in the form of nanorods and a fraction of crystals containing mixed-valence manganese oxide such as Mn_5O_8 and Mn_3O_4. The coexistence of these phases bestows special properties to this kind of composite materials, and it is the main factor responsible for the improvement in the catalytic behavior observed with the Ce/Mn oxide systems.

It is clear from the analysis of HREM images and XEDS spectra that the large and rounded oxide crystals (type A) correspond to pure α-Mn_2O_3. In spite of the similarities of the

α-Mn_2O_3 structure with the C-type Ln_2O_3 structure (β-Mn_2O_3), the lack of incorporation of lanthanide ions into the manganese oxide lattice may be explained if we consider the differences between the radius of Mn^{3+} and Ce^{3+} ions, 72 and 117 pm, respectively. Even Ce^{4+} (94 pm) is a cation too big to replace the small Mn^{3+} ions.

However, this is not the case for the type C nanocrystals. The reference framework for these crystals is the fluorite-like structure of CeO_2. The radius of the Mn^{2+} ion, 81 pm, is much closer to the radius of the Ce^{4+} cations. Therefore they can be incorporated into the fluorite lattice by substituting cerium cations and creating some oxygen vacancies, as has been described elsewhere.[65] One oxygen vacancy will be created by each manganese ion replacing a cerium ion. We could expect to have a small fraction of these manganese ions in a higher oxidation state, and probably also in a different defect position inside the fluorite like structure, as reported.[22]

The maximum content of manganese in type C nanocrystals detected by XEDS experiments is about 20% (molar percentage) in good agreement with other works.[22] This implies the existence of 10% oxygen vacancies if all the manganese ions replace cerium ions. This content of oxygen vacancies, which is very high, is very close to the one found in the iota phase (the most reduced intermediate phase for cerium oxide).[39] It can be inferred from these experiments that the limit in the solubility of manganese ions into the fluorite lattice may be due to the intrinsic limitations of the ceria fluorite lattice structure, among other factors. The existence of these vacancies and the possibility of oxygen exchange and transport through the sample may play an important role in the catalytic reactions, as proposed elsewhere.[17] Besides the intrinsic catalytic properties of these oxide nanocrystals, they could also work like a high specific area sponge, taking oxygen dissolved in water through their surface which could be then fed to the manganese oxides phases that lose oxygen during the catalytic reaction.[11] The coexistence of these two phases (A and C) could be the main factor responsible for the synergetic effect of Ce/Mn oxides during CWO reactions. This synergetic effect is maximum at a molar ratio close to 50/50 (see Figure 4), because this is the one that provides more opportunities for interactions between these two phases.

To understand the occurrence of γ-MnOOH nanorods in the fresh precipitates, a more detailed consideration of the chemical processes occurring during the coprecipitation from the solution containing Ce^{3+} and Mn^{2+} would be necessary. We have proven here that these nanorods can be transformed, following a topotaxial relationship,[14] to β-MnO_2 nanorods during the calcination treatment up to 500 °C. The absence of peaks that could be assigned to β-MnO_2 in the X-ray diffraction pattern of the calcined sample can be simply due to special morphology of these nanorods and their low concentration. However, the TEM images show the presence of nanorods for all studied Ce/Mn oxide samples, with the exception of CM100.

In spite of their low concentration, the occurrence of these β-MnO_2 nanorods where manganese ions are in oxidation state +4 may also play an important role during the catalytic reactions. Thus, the mechanism of synergy between MnO_2 and CeO_2 during the oxidation of NH_3 and reduction of NO, in the presence of oxygen, to produce nitrogen and water has been reported.[18,20] In this case, MnO_2 liberates oxygen, which participates in the oxidation of NH_3. The reduced MnO_2 is oxidized in a second step by the CeO_2 present in the sample.[11] In the case of the present work, the Ce/Mn mixed oxide nanocrystals may play this function. As we can see in Figure

9, there is a strong interaction between phases B and C. Again the molar ratio close to 50/50 is the one that provides also more opportunities for interactions between a pure manganese oxide, like β-MnO$_2$, and the only phase containing cerium.

There is another ingredient to consider in the discussion: the existence of mixed-valence manganese oxides. Mn$_5$O$_8$ may be formed, during the calcination at 500 °C, from a lower manganese oxide or through the oxidation of γ-MnOOH. In fact, a structural relationship between these two phases during the formation of β-MnO$_2$ nanorods has been previously described.[47] In general, the existence of crystals where manganese ions coexist in two different oxidation states, +2 and +4 in Mn$_5$O$_8$ or +2 and +3 in Mn$_3$O$_4$, is another unique feature of Ce/Mn composite oxides. In fact, a correlation between the chemical properties of the Ce/Mn oxides and the existence of manganese in more than one oxidation state has been argued.[10] However, taking into account that the maximum catalytic activity is achieved for a molar ratio close to 50/50, in which the fraction of mixed-valence manganese oxides is small compared with sample CM85, the only presence of mixed-valence manganese oxides cannot clearly explain the chemical behavior of the composite systems investigated in this work.

On the other hand, as shown in Figure 3, the presence of the Ce/Mn mixed oxide and the manganese(IV) oxide, responsible for the peaks in the TPR around 200 and 550−600 °C, respectively, could explain[25] the enhancement in the reducibility at low temperature of the Ce/Mn composite oxides with respect to pure manganese oxide. This property, related to the oxygen exchange capability of the system, will play an important role during the CWO reaction.

5. Conclusions

The coprecipitation method followed by calcination at 773 K allows preparing Ce/Mn oxide composites in which a variety of phases can coexist. Besides large and rounded crystals, made of α-Mn$_2$O$_3$, three other phases are present that contribute to enhance the catalytic performance of the system. Thus, a Ce/Mn solid solution mixed oxide nanocrystals with high specific area and high oxygen mobility may notably contribute to create a source of atomic oxygen to feed and boost other active manganese oxides during the catalytic oxidation of model phenol solutions at lower temperature. Likewise, the formation of β-MnO$_2$ nanorods with Mn in a high oxidation state may also contribute to an improvement during the CWO reaction. An additional, but in no case dominant, contribution in this respect could also come from the fourth component of these composites, the mixed-valence manganese oxides Mn$_3$O$_4$ and Mn$_5$O$_8$.

The maximum number of interactions between pure manganese oxide phases (α-Mn$_2$O$_3$ and β-MnO$_2$) and the only phase containing cerium in a very high proportion (the Ce/Mn mixed oxide) is achieved for a molar ratio close to 50/50. This explains the maximum synergetic effect in the catalytic activity obtained at this composition.

This work also illustrates that the combination of complementary electron microscopy techniques allows performing an in depth structural and chemical characterization of quite complex systems, as are clearly the composites considered in this work. The structure and chemical composition of the different phases present in these nanostructured materials, their final distribution, and the interaction between them can only be understood on the basis of spatially resolved techniques, as those used here, the knowledge of them being essential to rationalize the macroscopic behavior and catalytic activity of the Ce/Mn oxides systems.

Supporting Information Available: Table of HREM data. This material is available free of charge via the Internet at http://pubs.acs.org.

References and Notes

(1) Chen, H.; Sayari, A.; Adnot, A.; Larachi, F. *Appl. Catal. B: Environ.* **2001**, *32* (3), 195–204.
(2) Blanco, G.; Cauqui, M. A.; Delgado, J. J.; Galtayries, A.; Pérez-Omil, J. A.; Rodríguez-Izquierdo, J. M. *Surf. Interface Anal.* **2004**, *36* (8), 752–755.
(3) Delgado, J. J.; Pérez-Omil, J. A.; Rodríguez-Izquierdo, J. M.; Cauqui, M. A. *Catal. Commun.* **2006**, *7* (9), 639–643.
(4) Abecassis-Wolfovich, M.; Landau, M. V.; Brenner, A.; Herskowitz, M. *Ind. Eng. Chem. Res.* **2004**, *43* (17), 5089–5097.
(5) Silva, A. M. T.; Marques, R. R. N.; Quinta-Ferreira, R. M. *Appl. Catal. B: Environ.* **2004**, *47* (4), 269–279.
(6) Bhargava, S. K.; Tardio, J.; Prasad, J.; Foger, K.; Akolekar, D. B.; Grocott, S. C. *Ind. Eng. Chem. Res.* **2006**, *45* (4), 1221–1258.
(7) Levec, J.; Pintar, A. *Catal. Today* **2007**, *124* (3−4), 172–184.
(8) Abecassis-Wolfovich, M.; Landau, M. V.; Brenner, A.; Herskowitz, M. *J. Catal.* **2007**, *247* (2), 201–213.
(9) Arena, F.; Trunfio, G.; Negro, J.; Spadaro, L. *Appl. Catal. B: Environ.* **2008**, *85* (1−2), 40–47.
(10) Imamura, S.; Nakamura, M.; Kawabata, N.; Yoshida, J.; Ishida, S. *Ind. Eng. Chem. Prod. Rese. Dev.* **1986**, *25* (1), 34–37.
(11) Shi, L.; Chu, W.; Qu, F.; Luo, S. *Catal. Lett.* **2007**, *113* (1), 59–64.
(12) Tang, X.; Li, Y.; Huang, X.; Xu, Y.; Zhu, H.; Wang, J.; Shen, W. *Appl. Catal. B: Environ.* **2006**, *62* (3−4), 265–273.
(13) Zhou, G.; Shah, P.; Gorte, R. *Catal. Lett.* **2008**, *120* (3), 191–197.
(14) Imamura, S.; Shono, M.; Okamoto, N.; Hamada, A.; Ishida, S. *Appl. Catal. A: General* **1996**, *142* (2), 279–288.
(15) Tikhomirov, K.; Kröcher, O.; Elsener, M.; Wokaun, A. *Appl. Catal. B: Environ.* **2006**, *64* (1−2), 72–78.
(16) Qi, G.; Yang, R. T. *J. Catal.* **2003**, *217* (2), 434–441.
(17) Qi, G.; Yang, R. T. *J. Phys. Chem. B* **2004**, *108* (40), 15738–15747.
(18) Qi, G.; Yang, R. T.; Chang, R. *Appl. Catal. B: Environ.* **2004**, *51* (2), 93–106.
(19) Eigenmann, F.; Maciejewski, M.; Baiker, A. *Appl. Catal. B: Environ.* **2006**, *62* (3−4), 311–318.
(20) Ding, Z. Y.; Li, L.; Wade, D.; Gloyna, E. F. *Ind. Eng. Chem. Res.* **1998**, *37* (5), 1707–1716.
(21) Kaneko, H.; Miura, T.; Ishihara, H.; Taku, S.; Yokoyama, T.; Nakajima, H.; Tamaura, Y. *Energy* **2007**, *32* (5), 656–663.
(22) Murugan, B.; Ramaswamy, A. V.; Srinivas, D.; Gopinath, C. S.; Ramaswamy, V. *Chem. Mater.* **2005**, *17* (15), 3983–3993.
(23) Hussain, S. T.; Sayari, A.; Larachi, F. *Appl. Catal. B: Environ.* **2001**, *34* (1), 1–9.
(24) Delgado, J. J. Doctoral thesis, University of Cádiz, Spain, 2003.
(25) Zaki, M. I.; Hasan, M. A.; Pasupulety, L.; Kumari, K. *Thermochim. Acta* **1997**, *303*, 171–181.
(26) Stobbe, E. R.; de Boer, B. A.; Geus, J. W. *Catal. Today* **1999**, *47* (1−4), 161–167.
(27) Baur, W. H. *Acta Crystallogr., Sect. B* **1976**, *32*, 2200.
(28) Geller, S. *Acta Crystallogr., Sect. B* **1971**, *27*, 821.
(29) Jarosch, D. *Mineral. Petrol.* **1987**, *37* (1), 15–23.
(30) Sasaki, S.; Fujinoa, K.; Takeuchia, Y.; Sadanagaa, R. *Acta Crystallogr., Sect. B* **1980**, *36*, 904–915.
(31) Millar, R. W. *J. Am. Chem. Soc.* **1928**, *50*, 1875.
(32) Moore, T. E.; Ellis, M.; Selwood, P. W. *J. Am. Chem. Soc.* **1950**, *72*, 856.
(33) Frisch, S.; Sarrias, J.; Rousset, A.; Kulkarni, G. U. *Mater. Res. Bull.* **1998**, *33* (8), 1185–1194.
(34) Gillot, B.; El Guendouzi, M.; Laarj, M. *Mater. Chem. Phys.* **2001**, *70*, 54.
(35) Azzoni, C. B.; Mozzati, M. C.; Galinetto, P.; Paleari, A.; Massarotti, V.; Capsoni, D.; Bini, M. *Solid State Commun.* **1999**, *112* (7), 375–378.

(36) Oswald, H. R.; Wampetich, M. J. *Helv. Chim. Acta* **1967**, *50*, 2023–2034.

(37) Yamada, N. O., M. *Acta Crystallogr.* **1986**, *B42*, 58–61.

(38) Kohler, T.; Armbruster, T.; Libowitzky, E. *J. Solid State Chem.* **1997**, *133* (2), 486–500.

(39) Kang, Z. C. *Handb. Phys. Chem. Rare Earths* **2008**, *38*, 1–53.

(40) López-Cartes, C.; Pérez-Omil, J. A.; Pintado, J. M.; Calvino, J. J.; Kang, Z. C.; Eyring, L. *Ultramicroscopy* **1999**, *80* (1), 19–39.

(41) Kümmerle, E. A.; Heger, G. *J. Solid State Chem.* **1999**, *147* (2), 485–500.

(42) Bärnighausen, H.; Schiller, G. *J. Less Common Met.* **1985**, *110* (1–2), 385–390.

(43) Hernandez, J. C.; Hungria, A. B.; Perez-Omil, J. A.; Trasobares, S.; Bernal, S.; Midgley, P. A.; Alavi, A.; Calvino, J. J. *J. Phys. Chem. C* **2007**, *111* (26), 9001–9004.

(44) Kraus, W.; Nolze, G. *J. Appl. Crystallogr.* **1996**, *29*, 301–303.

(45) Bernal, S.; Botana, F. J.; Calvino, J. J.; López-Cartes, C.; Pérez-Omil, J. A.; Rodríguez-Izquierdo, J. M. *Ultramicroscopy* **1998**, *72* (3–4), 135–164.

(46) Pérez-Omil, J. A. http://www.uca.es/tem-uca, 2009.

(47) Rask, J. H.; Buseck, P. R. *Am. Mineral.* **1986**, *71*, 805–814.

(48) Zheng, D.; Sun, S.; Fan, W.; Yu, H.; Fan, C.; Cao, G.; Yin, Z.; Song, X. *J. Phys. Chem. B* **2005**, *109* (34), 16439–16443.

(49) Zhang, Y.; Liu, Y.; Guo, F.; Hu, Y.; Liu, X.; Qian, Y. *Solid State Commun.* **2005**, *134* (8), 523–527.

(50) Folch, B.; Larionova, J.; Guari, Y.; Guérin, C.; Reibel, C. *J. Solid State Chem.* **2005**, *178* (7), 2368–2375.

(51) Zhang, Y. C.; Qiao, T.; Hu, X. Y.; Zhou, W. D. *J. Cryst. Growth* **2005**, *280* (3–4), 652–657.

(52) Pennycook, S. J.; Boatner, L. A. *Nature* **1988**, *336* (6199), 565–567.

(53) Browning, N. D.; Chisholm, M. F.; Pennycook, S. J. *Nature* **1993**, *366* (6451), 143–146.

(54) Schmid, H. K.; Mader, W. *Micron* **2006**, *37* (5), 426–432.

(55) Kurata, H.; Colliex, C. *Phys. Rev. B* **1993**, *48* (4), 2102.

(56) Kurata, H.; Lefèvre, E.; Colliex, C.; Brydson, R. *Phys. Rev. B* **1993**, *47* (20), 13763.

(57) Mansot, J. L.; Leone, P.; Euzen, P.; Palvadeau, P. *Microsc., Microanal., Microstruct.* **1994**, *5*, 79.

(58) Cramer, S. P.; DeGroot, F. M. F.; Ma, Y.; Chen, C. T.; Sette, F.; Kipke, C. A.; Eichhorn, D. M.; Chan, M. K.; Armstrong, W. H. *J. Am. Chem. Soc.* **1991**, *113* (21), 7937–7940.

(59) Riedl, T.; Gemming, T.; Wetzig, K. *Ultramicroscopy* **2006**, *106* (4–5), 284–291.

(60) Pearson, D. H.; Ahn, C. C.; Fultz, B. *Phys. Rev. B* **1993**, *47* (14), 8471.

(61) Garvie, L. A. J.; Craven, A. J. *Ultramicroscopy* **1994**, *54* (1), 83–92.

(62) Du, G. H.; Yuan, Z. Y.; Van Tendeloo, G. *Appl. Phys. Lett.* **2005**, *86* (6), 063113−3.

(63) Rask, J. H.; Miner, B. A.; Buseck, P. R. *Ultramicroscopy* **1987**, *21* (4), 321–326.

(64) Wang, Z. L.; Yin, J. S.; Jiang, Y. D. *Micron* **2000**, *31* (5), 571–580.

(65) de Biasi, R. S.; Grillo, M. L. N. *J. Phys. Chem. Solids* **2003**, *64* (8), 1365–1369.

(66) Garvie, L. A. J.; Buseck, P. R. *J. Phys. Chem. Solids* **1999**, *60* (12), 1943–1947.

(67) Xu, H.; Wang, Y. *J. Nucl. Mater.* **1999**, *265* (1−2), 117–123.

(68) Paterson, J. H.; Krivanek, O. L. *Ultramicroscopy* **1990**, *32* (4), 319–325.

(69) Wang, Z. L.; Bentley, J.; Evans, N. D. *J. Phys. Chem. B* **1999**, *103* (5), 751–753.

(70) Djerdj, I.; Arcon, D.; Jaglicic, Z.; Niederberger, M. *J. Phys. Chem. C* **2007**, *111* (9), 3614–3623.

(71) Mc Murdie, G. *J. Res. Natl. Bur. Stand* **1948**, *41*, 589.

(72) Ross, C. R.; Rubie, D. C.; Paris, E. *Am. Mineral.* **1990**, *75* (11−12), 1249–1252.

(73) Bystroem, A. M. *Acta Chem. Scand* **1949**, *3*, 163–173.

(74) Schilling, O.; Dahn, J. R. *J. Appl. Crystallogr.* **1998**, *31*, 396–406.

(75) Johnson, C. S.; Dees, D. W.; Mansuetto, M. F.; Thackeray, M. M.; Vissers, D. R.; Argyriou, D.; Loong, C.-K.; Christensen, L. *J. Power Sources* **1997**, *68* (2), 570–577.

(76) Dronskowski, R.; Simon, A.; Miller, G.; Hettich, B.; Krebs, B. *Z. Anorg. Chem.* **1987**, *558*, 7–20.

(77) Christensen, A. N.; Ollivier, G. *Solid State Commun.* **1972**, *10* (7), 609–614.

(78) Glasser, L. S. D.; Ingram, L. *Acta Crystallogr., Sect. B* **1968**, *B24*, 1233–1236.

JP100635E